AGU PUBLICATIONS

JGR

Journal of Geophysical Research: Solid Earth

RESEARCH ARTICLE

10.1002/2015JB012536

Grain size distribution uncertainty quantification in volcanic ash dispersal and deposition from weak plumes

Federica Pardini[1], Antonio Spanu[1,2,3], Mattia de' Michieli Vitturi[1], Maria Vittoria Salvetti[4], and Augusto Neri[1]

[1]Istituto Nazionale di Geofisica e Vulcanologia, Sezione di Pisa, Pisa, Italy, [2]Scuola Normale Superiore di Pisa, Pisa, Italy, [3]Deutschen Zentrums fur Luft- und Raumfahrt, Cologne, Germany, [4]Dipartimento di Ingegneria Civile e Industriale, Università di Pisa, Pisa, Italy

Key Points:
- We investigated the impact of uncertainty on the initial GSD of ash on dispersal and deposition
- Uncertainty in the mean diameter reduces with increasing distance from source
- Uncertainty in GSD standard deviation is almost constant with distance from source in air (reduces on ground)

Supporting Information:
- Figures S1–S4 and caption for Movie S1
- Movie S1

Correspondence to:
M. de' Michieli Vitturi,
mattia.demichielivitturi@ingv.it

Citation:
Pardini, F., A. Spanu, M. de' Michieli Vitturi, M. V. Salvetti, and A. Neri (2016), Grain size distribution uncertainty quantification in volcanic ash dispersal and deposition from weak plumes, *J. Geophys. Res. Solid Earth*, *121*, 538–557, doi:10.1002/2015JB012536.

Received 17 SEP 2015
Accepted 10 JAN 2016
Accepted article online 14 JAN 2016
Published online 3 FEB 2016

Abstract We present the results of uncertainty quantification and sensitivity analysis applied to volcanic ash dispersal from weak plumes with focus on the uncertainties associated to the original grain size distribution of the mixture. The Lagrangian particle model Lagrangian Particles Advection Code is used to simulate the transport of inertial particles under the action of realistic atmospheric conditions. The particle motion equations are derived by expressing the particle acceleration as the sum of forces acting along its trajectory, with the drag force calculated as a function of particle diameter, density, shape, and Reynolds number. Simulations are representative of a weak plume event of Mount Etna (Italy) and aimed at quantifying the effect on the dispersal process of the uncertainty in the mean and standard deviation of a lognormal function describing the initial grain size distribution and in particle sphericity. In order to analyze the sensitivity of particle dispersal to these uncertain variables with a reasonable number of simulations, response surfaces in the parameter space are built by using the generalized polynomial chaos expansion technique. The mean diameter and standard deviation of particle size distribution, and their probability density functions, at various distances from the source, both airborne and on ground, are quantified. Results highlight that uncertainty ranges in these quantities are drastically reduced with distance from source, making them largely dependent just on the location. Moreover, at a given distance from source, the distribution is mostly controlled by particle sphericity, particularly on the ground, whereas in air also mean diameter and sorting play a main role.

1. Introduction

Pyroclastic particles dispersal is certainly one of the most complex and impacting phenomena produced by explosive volcanoes. In fact, depending on the particle size and properties, volcanic fragments can have a residence time in the atmosphere ranging from few minutes up to months or even years, and therefore, they can reach areas located thousands of kilometers away from the volcanic source [*Sparks et al.*, 1997; *Rose and Durant*, 2009]. The effects of volcanic ash on the environment are also numerous and can represent serious problems for the affected populations and the nearby territories. Human health, industrial activities, farms, and crops are some of the fields more heavily affected by this treat as well as transports, both terrestrial and in air, and communications networks [*Barsotti et al.*, 2010; *Durant et al.*, 2010; *Wilson et al.*, 2014].

As a consequence volcanologists have deeply investigated the nature of pyroclastic fall deposits, the properties of pyroclastic particles, and the physical processes that govern the dispersal dynamics [*Bonadonna et al.*, 2015; *Houghton and Carey*, 2015]. With this specific aim, a number of numerical models, based on different physical and numerical formulations, have been developed and applied for simulating the dispersal and deposition processes and to correlate them to the nature and properties of the associated ash clouds and deposits (see, for instance, the consensus document of the 2nd IUGG-WMO Volcanic Ash Dispersal and Civil Aviation [*Bonadonna et al.*, 2014] for a list of current ash dispersal models).

Despite such major efforts the accurate prediction of pyroclastic particle dispersal, as well as the precise reconstruction of past events, remains a major challenge due to several sources of aleatoric and epistemic uncertainty [*Bonadonna et al.*, 2014, 2015]. Some of them are associated to the unknown a priori textural properties of particles such as shape, sphericity, and density (despite that these properties can be well constrained after an eruption) and to the transient eruptive conditions of the pyroclastic mixture at the source;

some others are associated to the nonlinear dynamics of the atmospheric and dispersal processes and to the complex and still largely unknown mechanisms governing the microphysics and turbulence of this process.

Several investigations have been already carried out to analyze the influence of the main variables and parameters characterizing the dispersal process and the associated deposits. Some of these address the effect of key physical parameters or processes, such as that of *Bonadonna and Houghton* [2005], who investigated the effect of particle Reynolds number on the depositional dynamics, or the work by *Biass et al.* [2014], who investigated the effect of different aggregation models on the dispersal and sedimentation processes.

In some other cases the investigation has been carried out by wide exploration of the variable space and application of quantitative stochastic methods. This is the case, for instance, of *Scollo et al.* [2008], who investigated the influence of the main eruptive source parameters on the key features of two well-studied eruptions of Mount Etna (Italy) and Mount Ruapehu (New Zealand) by using an advection-diffusion model and sensitivity analysis, and the work of *Stefanescu et al.* [2014], who investigated, by ensemble forecast and Monte Carlo simulations, the effect of uncertainty affecting both source parameters and wind field in the simulation of ash dispersal of the 2010 Eyjafjallajökull eruption in Iceland.

In this work a Lagrangian particle dispersal model has been adopted to study the dispersal dynamics and deposition of pyroclastic fragments (with a Gaussian distribution in the ϕ range [−4, 6]) with the specific aim to quantitatively explore the extent that the uncertainty on particle sphericity and on the initial grain size distribution (GSD) of the pyroclastic mixture affects the airborne and ground GSDs. The dispersal code LPAC (Lagrangian Particles Advection Code) [*de' Michieli Vitturi et al.*, 2010] has been chosen to describe the dynamics of inertial, multisize, and nonspherical particles under the action of a realistic complex wind field, with a horizontal speed between 5 and 20 m/s and the presence of atmospheric instabilities. Simulations have been carried out for a weak plume case, with parameters representative of a recent eruption of Mount Etna and by adopting a nonhydrostatic mesoscale meteorological model for the definition of a realistic background flow field.

A full uncertainty quantification (UQ) and sensitivity analysis (SA) have been then carried out by adopting a generalized polynomial chaos expansion (PCEg) technique able, by greatly reducing the computational effort, to fully explore the parameter space by a large number of simulations. PCEg was first introduced by *Wiener* [1938], and it is a non-sampling-based method (in contrast to the Monte Carlo method) aimed at quantifying uncertainty in dynamical systems. Since its introduction, PCEg has been extensively applied to fluid and structural mechanics problems [e.g., *Xiu and Karniadakis*, 2002; *Isukapalli*, 1999], but just very few applications have been made to volcanological processes [e.g., *Dalbey et al.*, 2008; *Madankan et al.*, 2012; *de' Michieli Vitturi et al.*, 2015]. The code adopted to perform the UQ analysis is the DAKOTA toolkit (Design Analysis Kit for Optimization and Terascale Applications) [*Adams et al.*, 2006], an open-source software developed at Sandia National Laboratories providing a flexible and extensible interface between analysis codes (in our case the LPAC code) and iterative systems analysis methods (e.g., UQ, SA, optimization, and parameter estimation).

In the following, section 2 presents the main properties of the reference phenomenon investigated and section 3 presents the physical and numerical formulation of the LPAC code and the way the GSD of the mixture is represented. The details of the UQ and SA methods are briefly illustrated in section 4, whereas section 5 presents the results of some selected deterministic simulations as well as the main results of the stochastic analyses performed. Finally, section 6 reports a summary of the study and its main outcomes.

2. The Mount Etna Reference Event

The analysis presented in this work has been performed for dispersal conditions representative of the event of 24 November 2006, at Mount Etna, Italy (Figure 1). According to *Spinetti et al.* [2007] and *Andronico et al.* [2014], this eruption took place at the Southeast Crater, one of Mount Etna's summit craters, and it represented the most voluminous episode, in terms of mass of ash emitted, that occurred in 2006. This episode has been subdivided by *Andronico et al.* [2014] into three main eruption phases: resumption, paroxysmal, and conclusive. The resumption phase, which started at about 00:00 GMT on 24 November and was characterized by increasing degassing and sporadic ash emission, was the precursor of a paroxysmal phase that started at 2:00 GMT and stopped at 15:00 GMT, with a total duration of 13 h. The paroxysm consisted of powerful Strombolian activity and lava fountains, and it reached a peak between 12:00 and 13:00 GMT. During this event a weak volcanic plume rose up from the Southeast Crater reaching a maximum altitude of about 5 km above

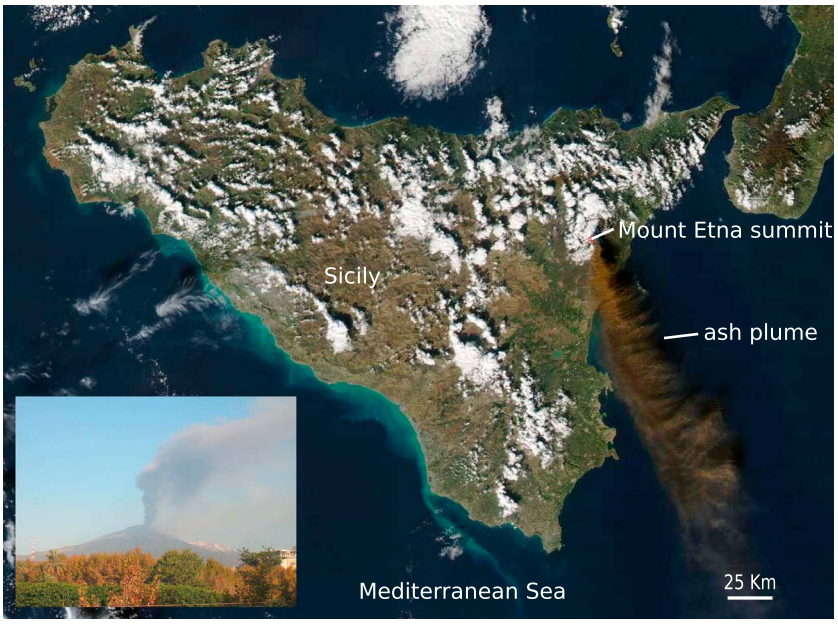

Figure 1. The 24 November 2006 eruption captured by the Moderate Resolution Imaging Spectroradiometer flying on board NASA's Aqua satellite (modified from http://eoimages.gsfc.nasa. gov/). In the inset is the volcanic plume as observed from the center of Catania at around 11:00 GMT (photo by Boris Behncke, INGV-Sezione di Catania).

sea level (asl); simultaneously, a tephra fallout covered the southeast and south flanks of Mount Etna. The paroxysmal phase was followed by a conclusive one in which the ash emission stopped between 16:00 and 17:00 GMT on 24 November 2006. The ash cloud showed characteristic horizontal stripes oriented perpendicularly to the prevailing wind direction (see Figure 1) as observed also at other volcanoes (e.g., Klyuchevskaya in Kamchatka and Eyjafjallajökull in Iceland). This phenomenon can be associated with Kelvin-Helmholtz (KH) atmospheric instabilities formed by interaction between the volcanic plume and the atmosphere [*Spanu et al.*, 2013]. In favorable conditions, the presence of the volcanic plume can in fact modify atmospheric temperature profile and allow the formation and growth of small atmospheric perturbations, perpendicular to the wind direction, in rolling waves similar to breaking oceans waves, as that which occurred, for example, in the eruption of 31 May 2012 at Popocatépetl volcano, Mexico.

The driving wind field used for the numerical simulations has been generated by WRF (Weather Research and Forecasting Model), a Eulerian fully compressible nonhydrostatic atmospheric model [*Skamarock et al.*, 2005]. Because the horizontal structures observed were oriented almost perpendicularly to the mean wind direction, and the wind direction was nearly constant after 12:00 GMT, we have investigated the phenomenon using two-dimensional simulations of the wind field. In particular, the Eulerian wind field was simulated over a domain of about 40 km horizontally and almost 6 km vertically, with the outputs saved each 10 min. It also covers a time interval of about 4 h. KH instabilities develop in the vertical range between 3300 and 4300 m asl approximately 1 h after the beginning of the Eulerian simulation. The plots of the wind velocity components (u_x, u_z) at two different instants of time are presented in Figure 2. Despite the characteristic and clear presence of KH instabilities in the Eulerian wind field, we have seen that these features do not significantly affect the uncertainty analysis and results presented in this work.

3. The Lagrangian Particle Model LPAC

For the analysis presented in this work we used a Lagrangian particle model, named LPAC [*de' Michieli Vitturi et al.*, 2010], to simulate the transport of pyroclastic particles under the action of the atmospheric field computed by the mesoscale model WRF, as explained in section 2. The equations of particle motion are derived expressing the Lagrangian acceleration as the sum of the forces acting along its trajectory. Using a simplified version of the Basset-Boussinesq-Oseen equation, the code allows to compute the trajectory of each particle by assuming a one-way coupling with the wind field in which the particle motion takes place. This means that while the properties of the background atmospheric field influence the motion of the

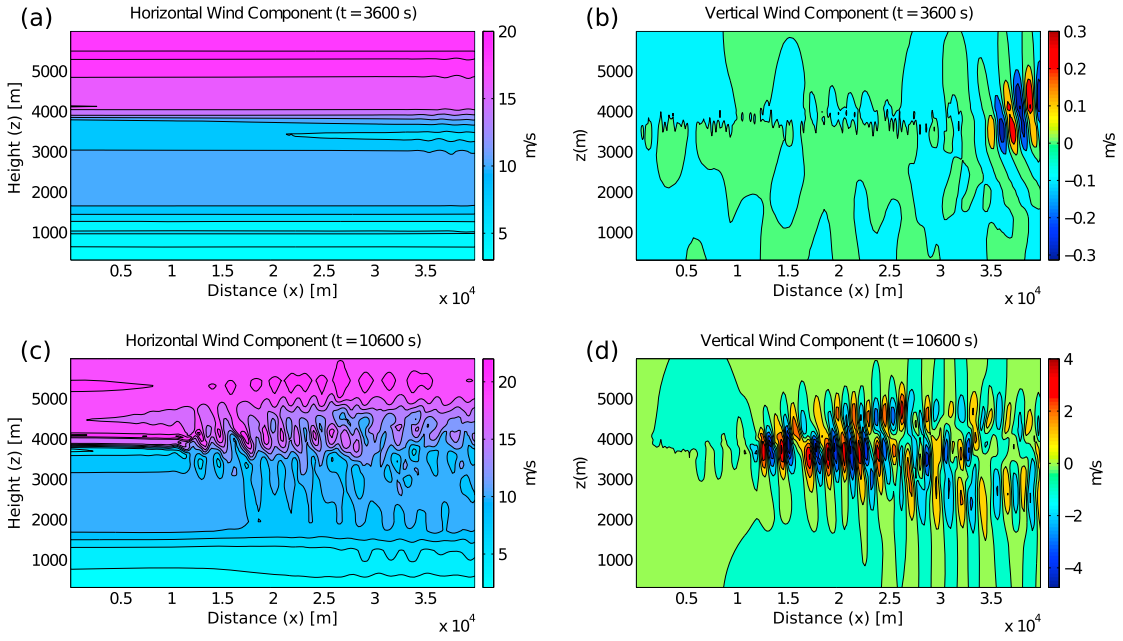

Figure 2. (a) Horizontal and (b) vertical components of the wind field plotted 1 h after the beginning of the Eulerian simulation. (c) Horizontal and (d) vertical components of the wind field plotted about 3 h after the beginning of the Eulerian simulation. A Kelvin-Helmholtz instability is found to originate in correspondence of the volcanic plume at ∼ 4000 m asl just after 1 h of simulation, due to the effect of a perturbation in the potential temperature profile simulating the presence of a volcanic cloud.

particles, the particles do not have an active effect on the characteristics of the wind field. This assumption is justified by the fact that particle concentration is low (approximately in the range 10^{-5}–10^{-6} kg/m^{-3}, according to *Corradini et al.* [2008]). Indeed, a momentum coupling parameter, Π_{mom}, defined as the ratio between the drag force F_D exerted by the particles on the fluid in a fixed volume and the momentum flux of the continuous phase through the volume, can be expressed as [*Crowe et al.*, 1998; *Sommerfeld et al.*, 2008]

$$\Pi_{mom} = \frac{C}{1+St}, \tag{1}$$

where C is the mass concentration and St the particle Stokes number. Therefore, the value of Π_{mom} is so small that the momentum coupling effects can be considered negligible and it is possible to adopt a one-way coupling between the Eulerian and the Lagrangian flow models. In addition, due to such low particle concentration in the ash cloud, collisions between particles can be neglected. For the same reason, aggregation and fragmentation processes were also not considered.

3.1. Equation of Motion

The motion equation of a particle in a steady flow at low Reynolds numbers is represented by the Basset-Boussinesq-Oseen (BBO) equation:

$$m_p \frac{d\mathbf{v}}{dt} = \mathbf{F_D} + \mathbf{F_P} + \mathbf{F_{Basset}} + \mathbf{F_{VM}} + \mathbf{F_G}. \tag{2}$$

The left-hand side of equation (2) represents the variation of momentum of a particle having a mass m_p and a velocity $\mathbf{v}$, while the right-hand side contains all the forces acting on the particle along its trajectory. These are the drag force, $\mathbf{F_D}$, the pressure gradient force, $\mathbf{F_P}$, the Basset force, $\mathbf{F_{Basset}}$ (this force accounts for the time lag associated to the chaining in the boundary layer), the virtual mass force, $\mathbf{F_{VM}}$ (associated to the inertia added to a particle due to the its acceleration in a fluid), and the body force, $\mathbf{F_G}$ (only the gravity force is here considered). If the moving particle has a diameter equal to D, the relative Reynolds number can be expressed as follows:

$$Re = \frac{D|\mathbf{u}-\mathbf{v}|}{\nu}, \tag{3}$$

where $\mathbf{u}$ and ν are the velocity and the kinematic viscosity of the carrier phase, respectively.

For the application presented in this work, it can be shown that some terms of the general BBO equation can be neglected. In particular, since the particles characteristic dimension is small compared to the characteristic dimension of the carrier flow, the Faxen correction and other flow curvature terms sometimes considered in the virtual mass force $\mathbf{F_{VM}}$ can be neglected [*de' Michieli Vitturi et al.*, 2010]. Also, the Basset history term $\mathbf{F_{Basset}}$ can be omitted; in fact, even if at low Reynolds number it increases the drag force, it has been demonstrated that its effects are less important than originally thought [*Dorgan and Loth*, 2007]. For these reasons equation (2) can be simplified as follows:

$$\begin{cases} \frac{dx}{dt} = v_x \\ \frac{dz}{dt} = v_z \\ \left(1+\frac{1}{2\gamma}\right)\frac{dv_x}{dt} = -C_D\frac{3}{4}\frac{|\mathbf{u}-\mathbf{v}|}{\gamma D}\left(u_x - v_x\right) + \frac{1}{2\gamma}\frac{du_x}{dt} - \frac{1}{\rho_p}\frac{dp}{dx} \\ \left(1+\frac{1}{2\gamma}\right)\frac{dv_z}{dt} = -C_D\frac{3}{4}\frac{|\mathbf{u}-\mathbf{v}|}{\gamma D}\left(u_z - v_z\right) + \frac{1}{2\gamma}\frac{du_z}{dt} - \frac{1}{\rho_p}\frac{dp}{dz} - g \end{cases}, \tag{4}$$

where v_x and v_z are, respectively, the horizontal and the vertical components of the velocity of the particle; u_x and u_z are the corresponding components of the wind velocity field in a Cartesian system, p is the pressure acting on the particle; and g is the gravity acceleration. The ratio between the density of the particle and the density of the fluid is herein expressed by $\gamma = \frac{\rho_p}{\rho_f}$.

3.2. Drag Coefficient

The main term controlling the coupling between the particles trajectories and the wind field is the drag force, and thus, a proper description of the drag coefficient C_D is required. However, the determination of the drag coefficient for spherical and nonspherical particles is a complicated and nonunivocally resolved task. It has been clearly shown that the drag coefficient of a particle is strongly related to its shape [e.g., *Wilson and Huang*, 1979], and thus recent studies have been focused on the development of new techniques in characterizing the shape and the size of volcanic particles [*Bagheri et al.*, 2015].

In this work we have chosen to express the C_D as a function of the Reynolds number, as defined in equation (3), and of the sphericity of the particle [*Ganser*, 1993]. The advantage of this choice lies in the relatively simple way to obtain an estimate of the C_D from the shape of the ash fragments. According to this approach, the differences in particle shapes are measured in terms of particle sphericity ψ, defined as the ratio of the surface area of a sphere with equivalent volume to the actual surface area of the particle:

$$\psi = \frac{\pi^{\frac{1}{3}}(6V_p)^{\frac{2}{3}}}{A_p}, \tag{5}$$

where V_p and A_p are the volume and the surface area of the particle, respectively; $\psi = 1$ means that the particle is a sphere.

To take into account both the extremely wide range of Reynolds numbers experienced by a particle during its motion and the shape of pyroclastic fragments, the Ganser formulation assumes that each isolated particle experiences (i) a Stokes regime in which drag is proportional to the relative velocity between the particle and the background fluid field and (ii) a Newton regime in which drag is proportional to the square of relative velocity. As a consequence, two shape factors are introduced: the Stokes shape factor, K_1, and the Newton shape factor, K_2.

In the case of *Stokes flow* (i.e., $Re \leq 0.05$), the drag coefficient can be expressed as [*Lee and Leith*, 1989]

$$C_D = \frac{4Dg(\rho_p - \rho_f)}{3v^2\rho_f} = \frac{24}{ReK_1}, \tag{6}$$

where v is the magnitude of the fluid velocity. The right-hand side expression in equation (6) is the usual Stokes law modified for nonspherical shapes with the introduction of the shape factor, K_1, modeled by *Lee and Leith* [1989] as a function of sphericity and expressed as follows:

$$K_1 = \left(\frac{1}{3} + \frac{2}{3}\psi^{-\frac{1}{2}}\right)^{-1}. \tag{7}$$

For the Newton regime (i.e., $Re \geq 1000$), the so-called Newton shape factor (K_2) is introduced through the equation [*Thompson and Clark*, 1991]

$$C_D = K_2 C_{DS}, \tag{8}$$

where C_D is the drag coefficient of nonspherical particles and C_{DS} is the drag coefficient of a sphere, both evaluated at a Reynolds number of 10^4.

Using experimental results, K_2 is estimated as a function of the sphericity as follows:

$$K_2 = 10^{1.8148(-log(\psi)^{0.5743})}. \tag{9}$$

Based on this approach, a simple expression of the C_D as a function of a generalized Reynolds number (ReK_1K_2) is proposed in *Ganser* [1993] for spherical and nonspherical particles and valid for $ReK_1K_2 \leq 10^5$, i.e.,

$$\frac{C_D}{K_2} = \frac{24}{ReK_1K_2}\left(1 + 0.1118(ReK_1K_2)^{0.6567}\right) + \frac{0.4305}{1 + \frac{3305}{ReK_1K_2}}, \tag{10}$$

where K_1 and K_2 have the expressions reported in equations (7) and (9), respectively. The power of equation (10) lies in his capability to estimate the drag coefficient over a wide range of Reynolds numbers as a function of sphericity. Such approach appears to be a good trade-off between ease of formulation and accuracy of results.

3.3. Numerical Discretization

The simplified set of equation (4) has been numerically integrated using a fourth-order Runge-Kutta method. In contrast with the original method presented in *de' Michieli Vitturi et al.* [2010], the drag term has been herein treated implicitly to improve the stability of the numerical scheme when using larger time steps. For the sake of simplicity, we present here just the implicit temporal discretization of the velocity equation for a first-order scheme, i.e.,

$$\left(1 + \frac{1}{2\gamma}\right)\frac{\mathbf{v}^{n+1} - \mathbf{v}^n}{\Delta t} = D_C\left(\mathbf{u}^n - \mathbf{v}^{n+1}\right) + O.T.\,, \tag{11}$$

where the terms

$$D_C = -C_D\frac{3}{4}\frac{|\mathbf{u} - \mathbf{v}|}{\gamma D} \qquad \text{and} \qquad O.T. = -\mathbf{g} - \frac{1}{\rho_p}\nabla p + \frac{1}{2\gamma}\frac{\mathrm{d}\mathbf{u}}{\mathrm{d}t} \tag{12}$$

are treated explicitly.

Rearranging the terms of equation (11), we obtain

$$\mathbf{v}^{n+1} = \frac{\left(1 + \frac{1}{2\gamma}\right)\mathbf{v}^n + \Delta t\left[D_C\mathbf{u}^n + O.T.\right]}{1 + \frac{1}{2\gamma} + D_C\Delta T}. \tag{13}$$

This equation allows to evaluate at each Runge-Kutta step k the changes in the velocity $\Delta\mathbf{v}_k = \mathbf{v}_k^{n+1} - \mathbf{v}_k^n$ that are combined linearly to produce the updated velocity at the new time step.

In addition to the implementation of an implicit scheme for the discretization in time, the LPAC code has been further developed through the implementation of a local time-stepping technique. In this technique, for each particle the global time step is divided into smaller local steps, dynamically reduced in order to avoid particles moving in two nonadjacent computational cells in a single local time step. Vice versa, if the particle remains in the same cell during the Runge-Kutta steps, the local time step is increased.

3.4. Grain Size Distribution

GSD is certainly one of the most important properties of volcanic particles, affecting their transport, dispersal, and deposition during the eruptive process. In this work the distribution of the pyroclastic particle size has been described by using the well-known logarithmic Krumbein scale expressed in ϕ units, defined as

$$\phi = -\log_2\left(\frac{D_{\mathrm{mm}}}{D_0}\right), \tag{14}$$

where D_{mm} is the grain diameter in millimeters and D_0 is a reference grain diameter equal to 1mm (please note that coarser particles are associated with smaller values of ϕ). In particular, the GSD of particles released from the volcanic plume, i.e., the mass distribution defined as a function of the diameter expressed in the Krumbein scale, has been assumed as Gaussian in the mass fraction and characterized by a mean diameter, μ_{in}, and a standard deviation, σ_{in}.

It is worth nothing that when dealing with volcanic particles, similar amount of mass of particles having a very different diameter in the Krumbein scale can be present in the atmosphere. This means, for example, that if the range of ash diameters covers a scale from 10^{-6} m to 10^{-3} m (i.e., from about 10ϕ to 0ϕ), the number of particles with a diameter equal to 10^{-6} m needed to obtain the same mass of a single particle of diameter 10^{-3} m is of the order of 10^9 (assuming the same density for the two particle sizes). Such number of particles results to be computationally unmanageable by any Lagrangian code. For this reason, we have not modeled individual particles but packages, or *parcels*, of particles assuming that all the parcels have the same mass. As a consequence, in the simulations presented in this work, each Lagrangian parcel released in the atmosphere is representative of a fixed amount of mass of pyroclastic material composed of a variable number of particles having the same size, similarly to what was done in *Barsotti and Neri* [2008]. Nevertheless, in order to have a proper statistical description of the GSD during the dispersal and deposition processes, the order of magnitude of the number of parcels simulated for each simulation is $\approx o(10^5)$.

Finally, particle density has been estimated as a function of the particle diameter, following the approach of *Bonadonna and Phillips* [2003]. Pumice particles, for the sake of simplicity, the only one taken into account in the present work, are highly vesicular fragments, so their density varies significantly with the size. Typically, smaller fragments, which are less vesicular, are more dense than the coarse ones. In detail, for smaller particles, i.e., those with a diameter greater than 7 in the ϕ scale, a density of 2500 kg/m^3 has been assumed, whereas for coarse fragments with a diameter smaller than 0 in the ϕ scale, a density of about 1000 kg/m^3 has been assumed. In the range $[7\phi, 0\phi]$ particle density has been assumed to linearly decreases from 2500 kg/m^3 to 1000 kg/m^3, this choice being based on previous studies for Etna eruptions [*Scollo et al.*, 2007, 2008]. In recent years, several other studies addressed the estimation of particle density as a function of particle size. In *Eychenne and Le Pennec* [2010], samples from the 2006 subplinian eruption of Tungurahua volcano in Ecuador are analyzed, suggesting a sigmoidal law for density of scoria and pumice with a plateau of 2600 kg/m^3 for clasts finer than 1.5ϕ. In *Douillet et al.* [2014], an almost constant density of 2500 kg/m^3 and 1400 kg/m^3 have been measured in the range $[3\phi, -4\phi]$ for scoria and pumice particles from the East Eifel volcanic area. Nevertheless, we remark that in *Scollo et al.* [2008], a sensitivity analysis quantifying the effect of several eruption parameters on tephra dispersal is presented, classifying particle density as a "noninfluential" parameter. This is also confirmed by additional analysis we performed, where different values for particles density have been tested producing similar uncertainty quantification results (see supporting information).

4. Uncertainty Quantification and Sensitivity Analysis Techniques

Atmospheric dispersal models are affected by numerous sources of uncertainty since their dynamics are largely controlled by nonlinear processes and by initial and boundary conditions that cannot be accurately predicted in advance. In this work UQ and SA have been performed to better describe the role and the effects of some of the uncertainties related to incomplete knowledge of the volcanological input parameters. In particular, we are interested in the uncertainties associated to the parameters representing the GSD of particles: the mean diameter (μ_{in}), the standard deviation (σ_{in}) of the particle size distribution, and the sphericity (ψ) of the particles.

4.1. Uncertainty Quantification Analysis

The technique adopted to perform the UQ analysis is the so-called generalized polynomial chaos expansion (PCEg), which is included within the class of stochastic expansion method. In the context of UQ, the term "chaos" simply refers to the uncertainty in the input, while the term "polynomial" is used because propagation of uncertainties to the outputs is described by reconstructing the output of the model through polynomials. Denoting with $\boldsymbol{\xi} = (\xi_{i_1}, \xi_{i_2}, \ldots, \xi_{i_n})$ the vector of input variables (n is the number of uncertain input variables) and with R the output of the model (response function), the first step to perform the "expansion" is to model the input variables through appropriate probability distributions. The polynomial reconstruction of the response function R can be written as follows:

$$R(\boldsymbol{\xi}) = a_0 B_0 + \sum_{i_1=1}^{\infty} a_{i_1} B_1(\xi_{i_1}) + \sum_{i_1=1}^{\infty} \sum_{i_2=1}^{i_1} a_{i_1 i_2} B_2(\xi_{i_1}, \xi_{i_2}) + \sum_{i_1=1}^{\infty} \sum_{i_2=1}^{i_1} \sum_{i_3=1}^{i_2} a_{i_1 i_2 i_3} B_3(\xi_{i_1}, \xi_{i_2}, \xi_{i_3}) + \ldots . \tag{15}$$

For practical applications, the polynomial expression of equation (15) must be truncated to a finite order P and it can be rewritten as

$$R(\boldsymbol{\xi}) \simeq \sum_{j=0}^{P} \alpha_j \Psi_j(\boldsymbol{\xi}). \tag{16}$$

In equation (16) every term of the expansion is composed of the product between a multivariate polynomial, $\Psi_j(\xi)$, and a coefficient, α_j, and there is a direct correspondence between $\alpha_{i_1 i_2 i_3,\ldots,i_n}$ and α_j and between $B_n(\xi_{i_1}, \xi_{i_2}, \ldots, \xi_{i_n})$ and $\Psi_j(\xi)$ (see equation (15)). A uniform probability distribution has been assumed for the parameters describing the initial GSD. For this reason, following the Akey scheme [*Adams et al.*, 2006], the polynomial basis used by DAKOTA to construct the output functions is a Legendre basis.

The main computational effort concerning the PCEg technique lies in the calculation of the coefficients α_j of the polynomial expansion:

$$\alpha_j = \frac{\langle R, \Psi_j \rangle}{\langle \Psi_j^2 \rangle} = \frac{1}{\langle \Psi_j^2 \rangle} \int R(\xi)\Psi_j(\xi)\mathrm{d}\xi. \tag{17}$$

To compute the integral in the right-hand side of equation (17), we have chosen to use a Gaussian quadrature procedure, which is a suitable technique for problems with a low number of input variables as our work is. Since no sources of anisotropy have been considered, the three dimensions of the problem, i.e., one for each input variable considered, have been treated in the same way and with the same number of quadrature points.

Once the expansion coefficients have been calculated, the polynomials are used as fast "emulators" of the response functions of the Lagrangian code, in order to evaluate the variation of the output values for a wide number of initial conditions, without running the simulations again.

4.2. Sensitivity Analysis

In addition, a variance-based SA was performed to quantify the global sensitivity indices of the response functions to the uncertain input parameters [*Adams et al.*, 2006]. In contrast with some investigations, where the term sensitivity is used in a local sense to denote the computation of the response derivatives at a certain point, here the term is used in a global sense, i.e., to denote the investigation of variability in the response functions. A large number of responses has been evaluated using the polynomial expansions to compute the Sobol indices S_i, i.e.,

$$S_i = \frac{\mathrm{Var}_{\xi_i}[E(R|\xi_i)]}{\mathrm{Var}(R)}, \tag{18}$$

where E denotes the expected value and Var the variance. With this notation, the numerator in equation (18) is the variance of the expectation of the output function conditional to the variation of the ith input variable, while the denominator is the variance of the output function. The index S_i represents how much of the variability of an output R can be assigned to the variability prescribed to the generic input parameter, ξ_i. In a similar way, it is also possible to take into account interactions between couples or triplets of input variables by calculating the indices of second or third order, respectively, as

$$S_{ij} = \frac{\mathrm{Var}_{\xi_{ij}}[E(R|\xi_{ij})]}{\mathrm{Var}(R)}, \qquad S_{ijk} = \frac{\mathrm{Var}_{\xi_{ijk}}[E(R|\xi_{ijk})]}{\mathrm{Var}(R)}. \tag{19}$$

5. Model Application and Simulation Results

5.1. Simulation Setup and Input Data

The simulation of particle dispersal and deposition has been carried out in a domain with a horizontal extension of about 40 km and a vertical one of about 6 km, as shown in Figure 3. To better investigate the distribution of the parcels during the process, the domain has been subdivided into four vertical stripes, and, in each stripe, a distinction between the particles still in the atmosphere and those deposited on the ground has been made, thus resulting in eight distinct subdomains (named Air 1–4 and Ground 1–4). Such a subdivision of the domain clearly affects the GSDs estimated by the model. However, it allows to have in each subdomain a number of parcels sufficient to accurately estimate the statistical parameters of the GSDs and at the same time to represent the main trends and dependencies of these values with distance from the source. The inlet portion of the left-hand side boundary of the domain represents the region from which the parcels are released. Given the bent geometry of the Etna plume of 24 November 2006, the inlet is representative of the plume conditions at about 2 km from the source along the direction of the wind. In other words the inlet represents the portion of the eruptive column from which ash particles are released into the ash cloud. We assumed that the inlet extends 1 km vertically, from 3300 up to 4300 m asl. The Lagrangian simulation covers a time interval of 2 h, starting 1 h after the beginning of the Eulerian simulation carried out with WRF. Despite the eruptive event of 24 November 2006 lasting about 13 h, we have seen after about 2 h that a quasi steady state of the

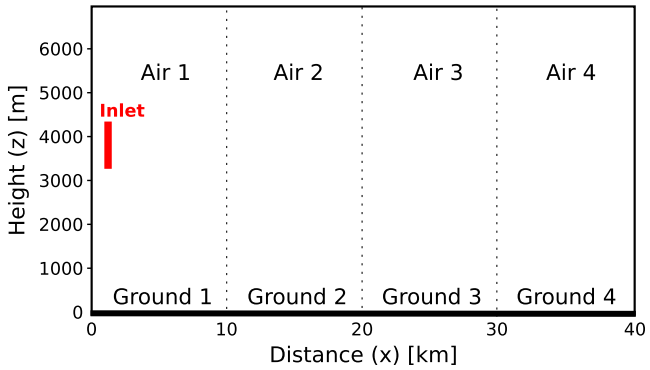

Figure 3. Sketch of the computational domain in which the ash dispersal and deposition processes take place. The ash particles are released from an inlet region of the left-hand side boundary with zero velocity and are uniformly distributed. The domain is partitioned into eight domains resulting from the division of the whole domain into four atmospheric subdomains (Air 1–4) and four ground subdomains (Ground 1–4).

aerial dispersal process is reached, and therefore this was assumed a sufficient time to estimate the mean and the standard deviation of the GSD over the assumed domain, while the loading on the ground would increase proportionally (considering a constant intensity of the wind). As mentioned above, KH instabilities are well developed and they are approximately located in the same vertical range of the inlet (3300–4300 m). The parcels are steadily released from the inlet every 10 s and every 50 m over the inlet section, with an initial velocity set equal to 0. This assumption on the initial velocity of the Lagrangian parcels is not restrictive because, due to the small size of ash particles, the time required to reach a coupling with the wind field is small compared to the residence time in the considered atmospheric domain. We also remark that in this study we have considered only particles released from the top of the plume and not particles lost from the edges of the eruptive columns during their rise in the atmosphere, which would affect the grain size distribution in the very proximal region.

Since the dispersion and deposition of volcanic ash are mainly influenced by the GSD, the uncertain input parameters we have chosen to investigate in this work are (1) the mean value of the initial GSD (μ_{in}), (2) the standard deviation of the initial GSD (σ_{in}), and (3) the sphericity of particles (ψ).

The choice of the ranges of variation of μ_{in} and σ_{in} has been made on the basis of the information reported in literature about the reconstruction of the total GSD of weak plumes events at Mount Etna [*Andronico et al.*, 2008a, 2008b, 2014; *Scollo et al.*, 2007; *Barsotti and Neri*, 2008; *Barsotti et al.*, 2010]. Since the aim of this study is to explore how the uncertainty on the original GSD affects the estimates of the GSD in the air and deposits, we have defined variability ranges of the parameters able to cover their reconstructed variability as computed for this type of events. For the sake of simplicity, we have also assumed the distribution of the parameters to be uniform so that the mode and the mean values of the size distribution are equal and the initial value of the skewness and kurtosis are equal to 0. Under these assumptions, we have chosen an initial normal distribution in the Krumbein scale with a range of variations of the mean diameter (μ_{in}) from 0ϕ to 2ϕ and a range of variations of its standard deviation (σ_{in}) from 1.3ϕ to 1.7ϕ. In addition, in order to evaluate the effect of the particle nonsphericity on the dispersal process, a range of ψ variation between 0.5 and 0.9 was assumed. This range of variations corresponds to the measurements presented in *Bagheri et al.* [2015], where it is shown that the sphericity of lapilli (2 mm $< d <$ 64 mm) is larger (0.65–0.9) than that of ash particles (0.5–0.8). Here in order to quantify independently the effects of sphericity from those of other parameters, and to simplify the analysis, the same value was associated to all particles sizes in each simulation carried out.

5.2. Results of Deterministic Simulations

Before carrying out the full UQ analysis, the results of a few Lagrangian simulations are illustrated. Figure 4 shows the particle distribution after 2 h from the beginning of parcels release, for a simulation with $\mu_{in} = 1\phi$, $\sigma_{in} = 1.5\phi$, and $\psi = 0.7$ (corresponding to the mean values of the parameter ranges described in the previous section), with different colors representing parcels of particles of different size (red the smallest particles and cyan the largest ones). Figure 4 (middle and bottom rows) shows the histograms of the size of the particles in the four atmospheric subdomains (middle row, Air 1–4 of Figure 3) and in the ground subdomains (bottom row, Ground 1–4 of Figure 3). In each panel the mean diameter and the standard deviation of the GSD are also

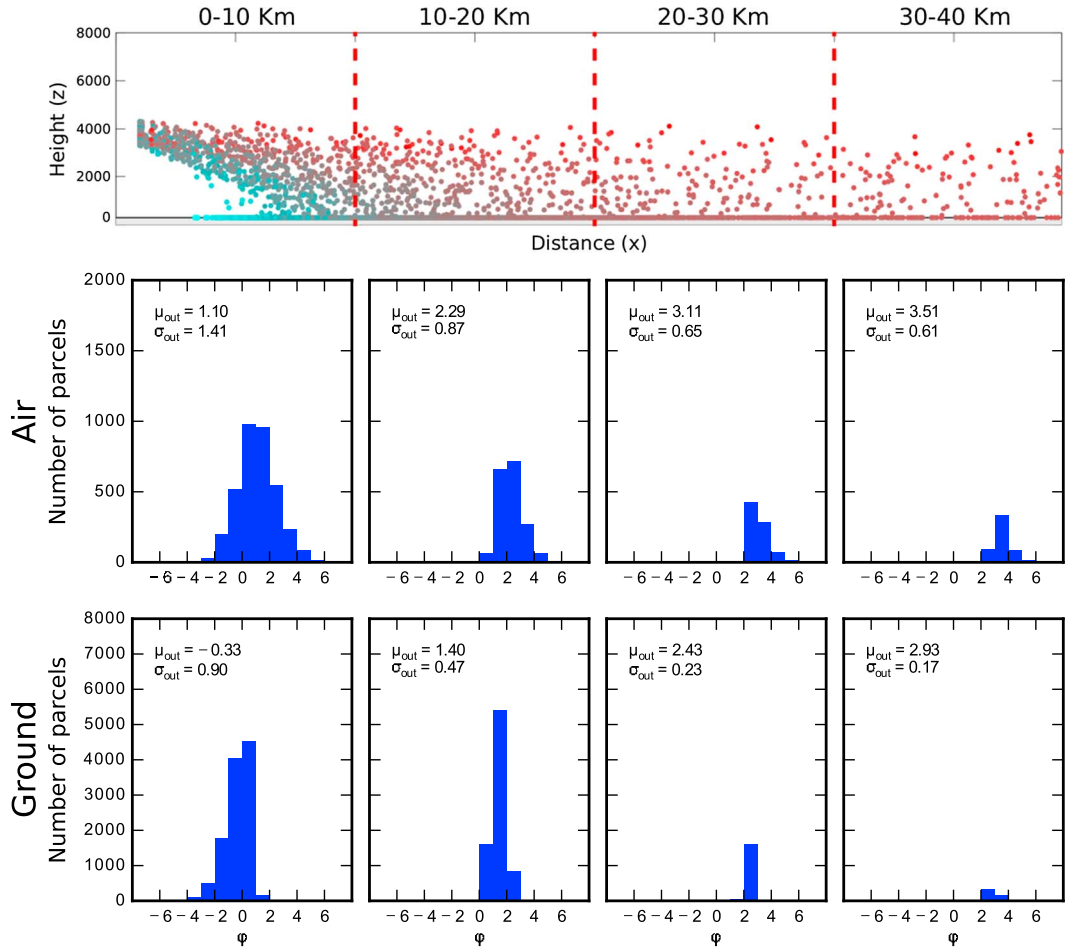

Figure 4. (top row) Distribution of parcels in the atmosphere 2 h after the beginning of the parcels release. The color is representative of the size of the particles: in cyan are shown larger particles and in red smaller particles. (middle and bottom rows) GSD in the eight subdomains analyzed 2 h after the beginning of the dispersal process. Each plot reports the number of particles as a function of the ϕ scale. Each plot reports also the mean and standard deviation of the corresponding GSD.

reported. We can observe that the GSD strongly depends on the distance from the source and that even at the same distance from the source, the distributions in the atmosphere and on the ground can be significantly different. It is evident how the GSD becomes significantly more fine grained and well sorted with the increase of distance from the source. In particular, at constant distance from the source, the GSD in the atmospheric subdomain is finer and less sorted compared to the GSD on the ground. Finally, we can see how only the distribution in the aerial subdomains closer to the release (Air 1) is representative of the original one.

Three additional deterministic simulations were carried out by varying only one parameter at a time. Keeping σ_{in} and ψ constant and equal to their mean value, Figure 5 shows, again 2 h after the beginning of the release, the parcels dispersal for three different values of μ_{in} (spanning the whole considered variability interval μ_{in} [0ϕ, 2ϕ]). From the plots it is possible to observe again that the mean values of the GSD calculated in all the subdomains, with the only exception of the aerial subdomain closest to the source (Air 1 subdomain in Figure 3), do not significantly depend on the original mean grain size of the particles released in the atmosphere but instead largely depend on the distance from the source. Such a dependence is particularly evident for the GSD computed on the ground whose mean value is almost independent of the mean value of the initial GSD. Consequently, the mean grain size measured in the air or on the ground in a particular subdomain is not representative at all of the initial one. In contrast, it is possible to observe that the number of parcels, of each size and in total in each subdomain, significantly depends on the mean size of the initial distribution. As expected, when μ_{in} is decreased, which means increasing the amount of coarser particles in the inlet flow, the number of parcels in the aerial and ground subdomains closest to the release increases, whereas the number

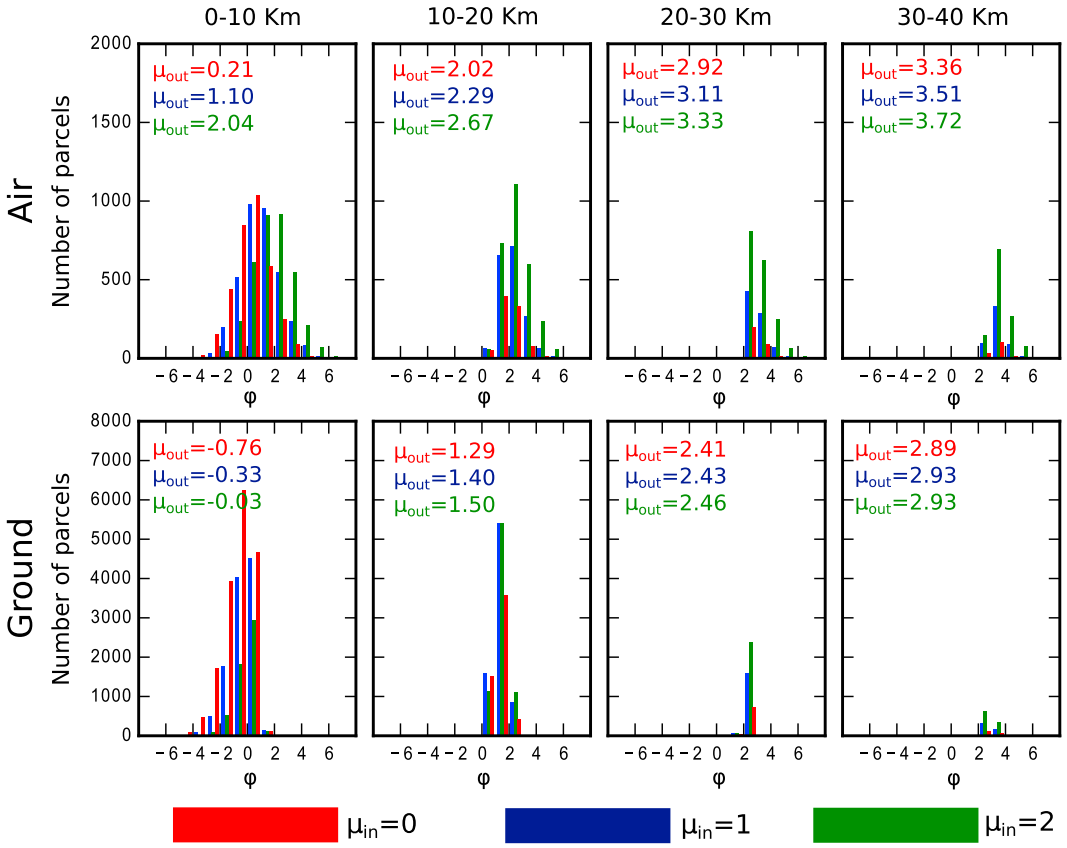

Figure 5. Histograms of the parcel size distributions as computed in the eight subdomains 2 h after the beginning of the parcels release. (top row) The aerial subdomains and (bottom row) the ground subdomains. The colors refer to the mean values of the GSDs considered and are equal $\mu_{in} = 0\phi$ (red), $\mu_{in} = 1\phi$ (blue), and $\mu_{in} = 2\phi$ (green). All simulations assume $\sigma_{in} = 1.5\phi$ and $\psi = 0.7$ (mean values of the ranges considered). In each plot are also reported the values of the mean parcel diameters (μ_{out}) as computed by varying the inlet mean diameter (μ_{in}). Please note that the GSDs plotted in blue are the same plotted in Figure 4 but with a different number of bins.

of parcels in the other subdomains and the number of parcels able to reach the right-hand side boundary of the domain decrease. In addition, considering that the same amount of parcels (and thus of mass) is released during the three simulations, it is shown that when the mean diameter of the input distribution varies from $\mu_{in} = 0\phi$ to $\mu_{in} = 2\phi$, the mass of parcels deposited on the ground decreases by about 30% (from 85% to 60% of the mass released), whereas the mass still in the atmosphere (in the considered domain) is almost doubled (plus about 95%).

The effects of the variation of the standard deviation of the initial GSD of the mixture are shown in Figure 6 in the same way as adopted in Figure 5. In this case the effects of the variation are much smaller. In fact, even if the initial sorting of the distribution shifts from 1.3ϕ to 1.7ϕ, it is evident that there are no significant variations in the parcels size distribution both in air and on the ground.

Finally, the variation of particle sphericity in the range [0.5, 0.9] was investigated keeping all other parameters equal to their mean value (see Figure 7). Similarly to the previous cases, it was shown that the characteristics of the initial GSD are maintained only in the aerial subdomain close to the source (Air 1), whereas in the other subdomains there is a quite evident change in particles size distribution. It is possible to observe also that the increase of particle sphericity (implying a reduced drag and thus a lower capacity of the fluid to transport the particles) does not significantly affect the total number of parcels present in the whole domain (almost 100% of those initially released), but it has an important effect on the size of the particle present in each of the subdomains. This effect is clearly reflected in the wider variation of the mean value of the GSD of the mixture at a given distance from the source (both on ground and in air).

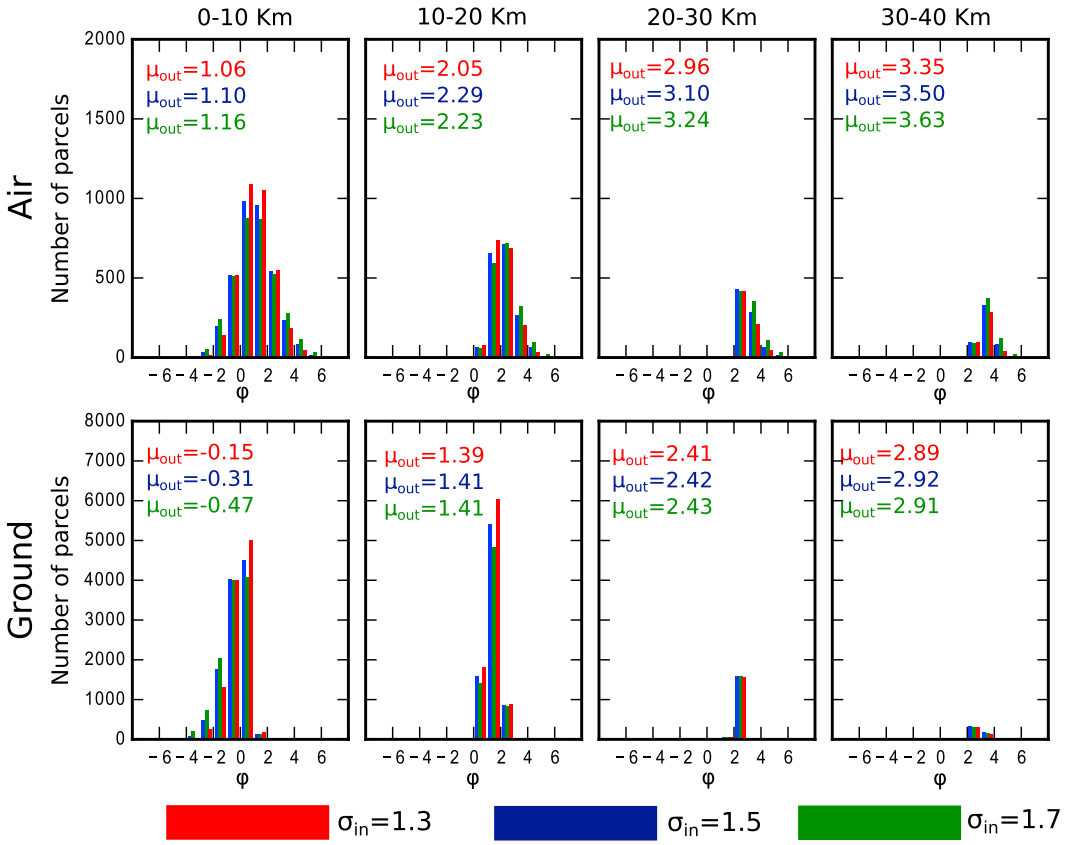

Figure 6. Histograms of the parcel size distributions as computed in the eight subdomains 2h after the beginning of the parcels release. (top row) The aerial subdomains and (bottom row) the ground subdomains. The colors refer to the mean values of the GSDs considered and are equal to $\sigma_{in} = 1.3\phi$ (red), $\sigma_{in} = 1.5\phi$ (blue), and $\sigma_{in} = 1.7\phi$ (green). All simulations assume $\mu_{in} = 1\phi$ and $\psi = 0.7$ (mean values of the ranges considered). In each plot are also reported the values of the mean parcel diameters (μ_{out}) as computed by varying the inlet standard deviation (σ_{in}). Please note that the GSDs plotted in blue are the same plotted in Figure 4 but with a different number of bins.

5.3. Uncertainty Quantification Results

While the results presented in section 5.2 give a first estimate of the dependence of the GSD on the three investigated parameters characterizing the initial GSD, a UQ analysis is needed to obtain a full picture of the variability of the results and their sensitivities on the three input parameters.

As previously said, the UQ analysis has been performed by using a PCEg method. Three input variables have been considered (μ_{in}, σ_{in}, and ψ), and a uniform probability distribution was assumed for each of them. The outputs have been analyzed at different times but are here reported just after 2h since the beginning of the Lagrangian simulation due to their full representativeness.

The quadrature order has been decided varying the number of quadrature abscissas until a convergence has been reached. We started from a quadrature order of 3, and we stopped at a quadrature order of 7. For the application presented in this work, good results are reached even with the lowest quadrature order. In fact, by using a quadrature order of 3 or higher, the response values do not significantly change and the error committed, passing from a quadrature order of 3 to a quadrature order of 7, is approximately 0.001%.

The polynomials computed with the PCEg technique have been used to evaluate the variation of the output values for a large number of initial conditions. In particular, 10,000 samples have been evaluated on the expansion for a likewise number of random input triplets to compute the cumulative distribution functions of the probabilities of the parameters describing the grain size in the eight subdomains of interest. In detail, seven cumulative probability levels (0.01, 0.05, 0.25, 0.5, 0.75, 0.95, and 0.99) have been fixed and mapped into the corresponding response levels.

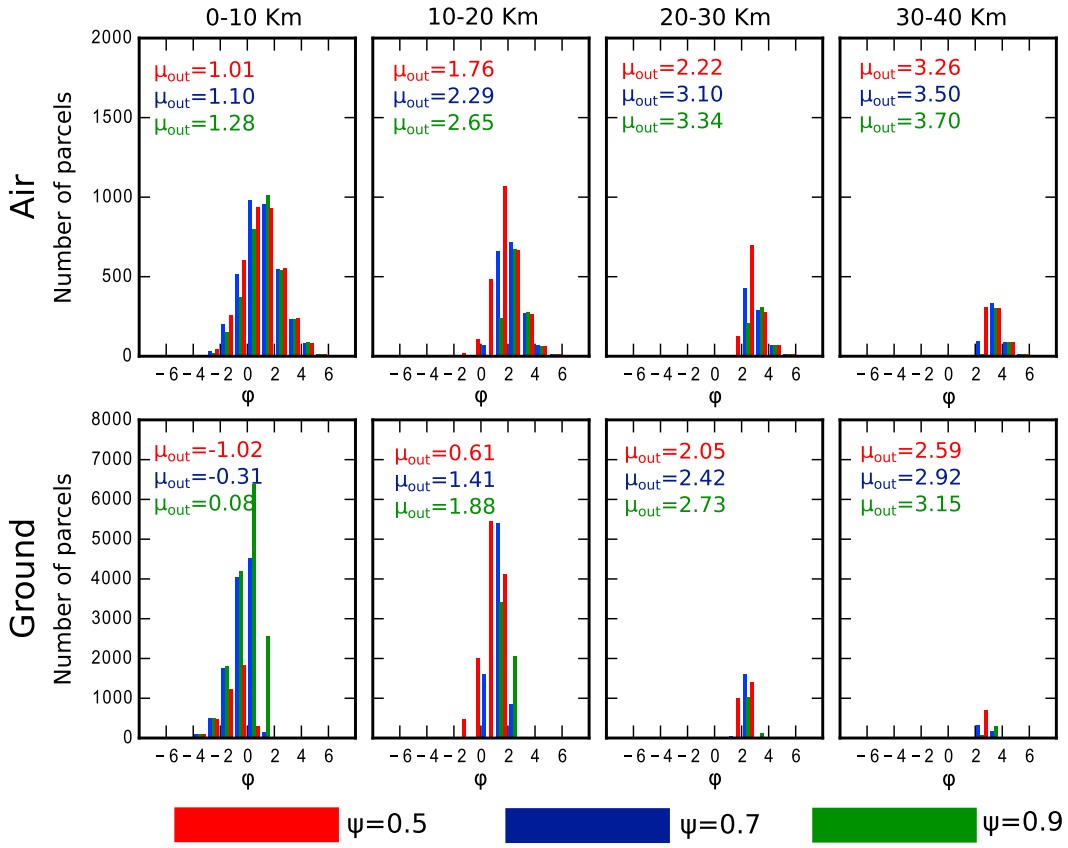

Figure 7. Histograms of the parcel size distributions as computed in the eight subdomains 2 h after the beginning of the parcels release. (top row) The aerial subdomains and (bottom row) the ground subdomains. The colors refer to the mean values of the GSDs considered and are equal to $\psi = 0.5$ (red), $\psi = 0.7$ (blue), and $\psi = 0.9$ (green). All simulations assume $\mu_{in} = 1\phi$ and $\sigma_{in} = 1.5\phi$ (mean values of the ranges considered). In each plot are also reported the values of the mean parcel diameters (μ_{out}) as computed by varying the particle sphericity (ψ). Please note that the GSDs plotted in blue are the same plotted in Figure 4 but with a different number of bins.

Figure 8 shows the stochastic probability distribution functions (PDFs) and the cumulative distribution functions (CDFs) of the mean diameter of the GSD (μ_{out}) expressed in the Krumbein scale and computed in each of the eight subdomains, both in the air and on the ground. In each plot the red curve represents the initial uncertainty distribution, which has been set as uniform over the range [0ϕ, 2ϕ] (please note that the blue curves in Figure 8a are not grain size distributions).

From Figure 8 it is possible to observe that the uncertainty affecting μ_{in} is reflected only in the most proximal aerial subdomain (Air 1), whereas, moving away from the inlet, the mean diameter not only becomes smaller but also the original uncertainty affecting it is lost. This is well evident from the distribution of the PDFs histograms of the mean diameter which are shifted to higher values of μ_{out} (which means finer particles according to the Krumbein scale) and whose dispersion decreases moving away from the inlet. Similarly, the CDFs, moving away from the source, tend to become steeper and they are more peaked around a particular value of μ_{out}, which increases moving downstream. For the specific eruptive conditions considered here, the best representation of the variability of μ_{in} can be observed on the ground from 10 to 20 km from the source (Ground 2).

In order to fully describe the effect of the uncertainty on the GSD at the source, it is also important to investigate the role of the sorting of parcels, which is representative of the dispersion of the particle dimensions around the mean value. In Figure 9 the PDFs and the CDFs of the standard deviation of the parcels distributions in the subdomains considered are reported, when a uniform PDF over the range [1.3ϕ, 1.7ϕ] (red curves in the figures) has been assumed for σ_{in} at the release location. Once the parcels are released and transported in the domain, we observe that only the aerial subdomain closest to the source preserves the original poor sorting variability, whereas in the other seven subdomains the parcels distributions tend to become

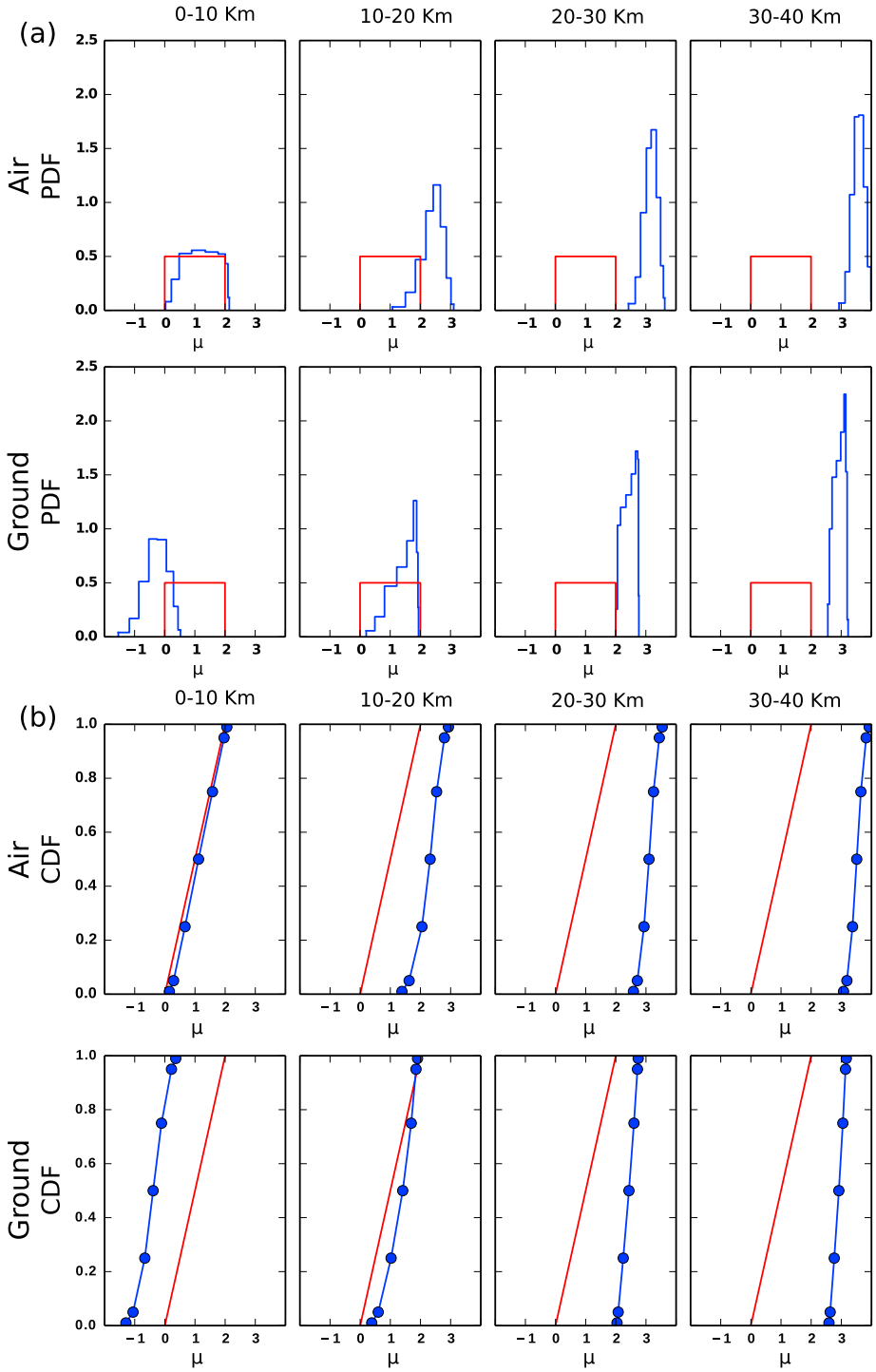

Figure 8. (a) Probability distribution functions (PDFs) and (b) cumulative distribution functions (CDFs) of the mean diameter of the parcels size distributions in each subdomain. (top row) Subdomains Air 1–4 and (bottom row) subdomains Ground 1–4. The red lines represent the distributions at the inlet, while the blue lines represent the distributions computed in the subdomains. Blue dots have been added to the CDFs for the 5, 25, 50, 75, and 95% probability levels. Please note that the curves in Figure 8a are not grain size distributions but probability distributions of the mean diameter μ_{out} when uncertainty in μ_{in}, σ_{in}, and ψ is considered.

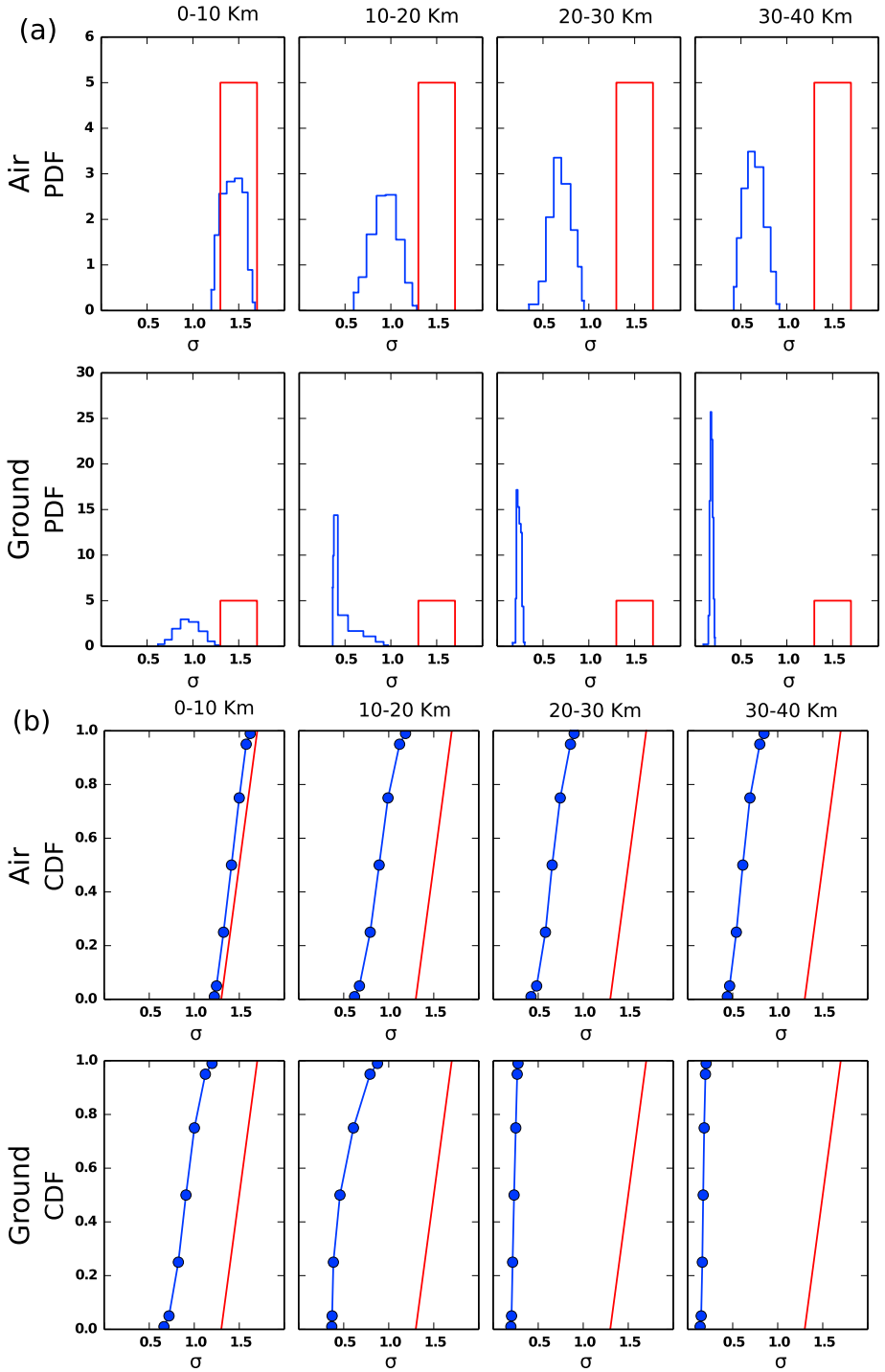

Figure 9. (a) Probability distribution functions (PDFs) and (b) cumulative distribution functions (CDFs) of the standard deviation of the parcels size distributions in each subdomain. (top row) Subdomains Air 1–4 and (bottom row) subdomains Ground 1–4. The red lines represent the distributions at the inlet, while the blue lines represent the distributions computed in the subdomains. Blue dots have been added to the CDFs for the 5, 25, 50, 75, and 95% probability levels. Please note that the curves in Figure 9a are not grain size distributions but probability distributions of the standard deviation σ_{out} when uncertainty in μ_{in}, σ_{in}, and ψ is considered.

Table 1. Mean Value and Standard Deviation Referred From the PDFs Associated to the Number of Parcels (*N*) Present in Every Subdomain[a]

	Air 1	Air 2	Air 3	Air 4	Ground 1	Ground 2	Ground 3	Ground 4
N mean value	3,517	1,843	907	593	10,693	7,693	1,689	525
N standard deviation	182	693	489	338	4,807	2,164	656	259

[a]Values of number of parcels refer to the distributions 2 h after the beginning of the dispersal process.

moderately sorted; i.e., the standard deviation values decrease. In more detail, it is possible to say that moving away from the release, the aerial GSDs become finer and more sorted, even if a significant dispersion of the sorting is retained. Vice versa, on the ground the situation is quite different, since not only the input variability is rapidly lost (the deposit is moderately sorted from 0 to 10 km from the source and becomes well sorted at larger distances), but, differently from the air, the slope of the CDFs curves, moving away from the inlet, becomes almost vertical. From a field perspective this means that while it is possible to approximately reconstruct the input main diameter of the GSD by sampling the deposit at a specific distance from the source (Ground 2, i.e., from 10 to 20 km from the inlet for the conditions here assumed), the input standard deviation cannot be detected from any specific location of the deposit. In order to retrieve the input standard deviation of the GSD at the inlet, it is therefore necessary to take into account the overall ash deposit and, even in this case, that the lack of information on the particles still suspended in the atmosphere can compromise the accuracy of the extrapolation. Vice versa, the results confirm that the GSD on ground is a strong function of distance from the source and is characterized by decreasing uncertainty moving away from the inlet, in terms of both mean value and standard deviation. In addition to the uncertainty analysis performed for the mean and the standard deviation of the parcels distributions in the subdomains considered, the skewness of the grain size distributions have also been analyzed (see supporting information). In this case, we observe that Ground 1–4 GSDs are negatively skewed (toward coarse particles), while Air 1–4 GSDs are positively skewed (toward fine particles), with skewness increasing with increasing distance from the release.

Finally, it is useful also to analyze how the variability in the initial GSD affects the number of parcels *N* transported in the different regions of the investigated domain. Table 1 reports the mean values and standard deviation of the number of parcels computed in the eight subdomains 2 h after the beginning of the dispersal. From the results, we can see that the number of the parcels in the air and on the ground decreases and loses variability moving away from the inlet. The only exception is represented by the standard deviation computed in the subdomain Air 1 that is the closest to the source. It is important to be reminded that the values reported in the table do not refer to the effective number of ash particles but to the number of particle parcels and thus correspond to the amount of mass. For this reason, the values reported in the table can be used to understand how the total ash mass has been transported and deposited in the domain. Considering the total number of parcels released during the simulation (about 30,000 over 2 h), and having supposed that all the parcels have the same mass, it can be computed that 2 h after the beginning of the release, about 75% of the total mass still in the domain is deposited on the ground, whereas the remaining 25% is still in the air. It was also estimated that about 10% of the total mass released has left the domain from the right-hand side boundary. This confirms again the fact that the information about the GSD of the parcels still in the atmosphere is fundamental in order to retrieve an accurate initial GSD of the ash released from the volcanic plume.

5.4. Sensitivity Analysis Results

In order to have a clearer view of the dependence of the output variability on the uncertainty affecting the source GSD, a global SA was also performed. As mentioned above, the PCEg technique allows to use the polynomial output functions as emulators of the Lagrangian code. In this way it was possible to perform an extremely high number of Lagrangian results (about 10,000 samples) needed to perform the SA simply using the polynomials.

The bar plots in Figure 10 show the main Sobol indices for the different output quantities up to the third order of interaction, as defined by equations (18) and (19). This means that not only the effect of each input parameter on the variability of output quantities is considered, but also all the possible interactions between the three input parameters are taken into account.

The plots show, overall and in a clear way, the leading role of the initial mean diameter of the GSD (μ_{in}) and of its sphericity (ψ).Thecontribution of the initial standard deviation (σ_{in}) is important just in the aerial subdomain

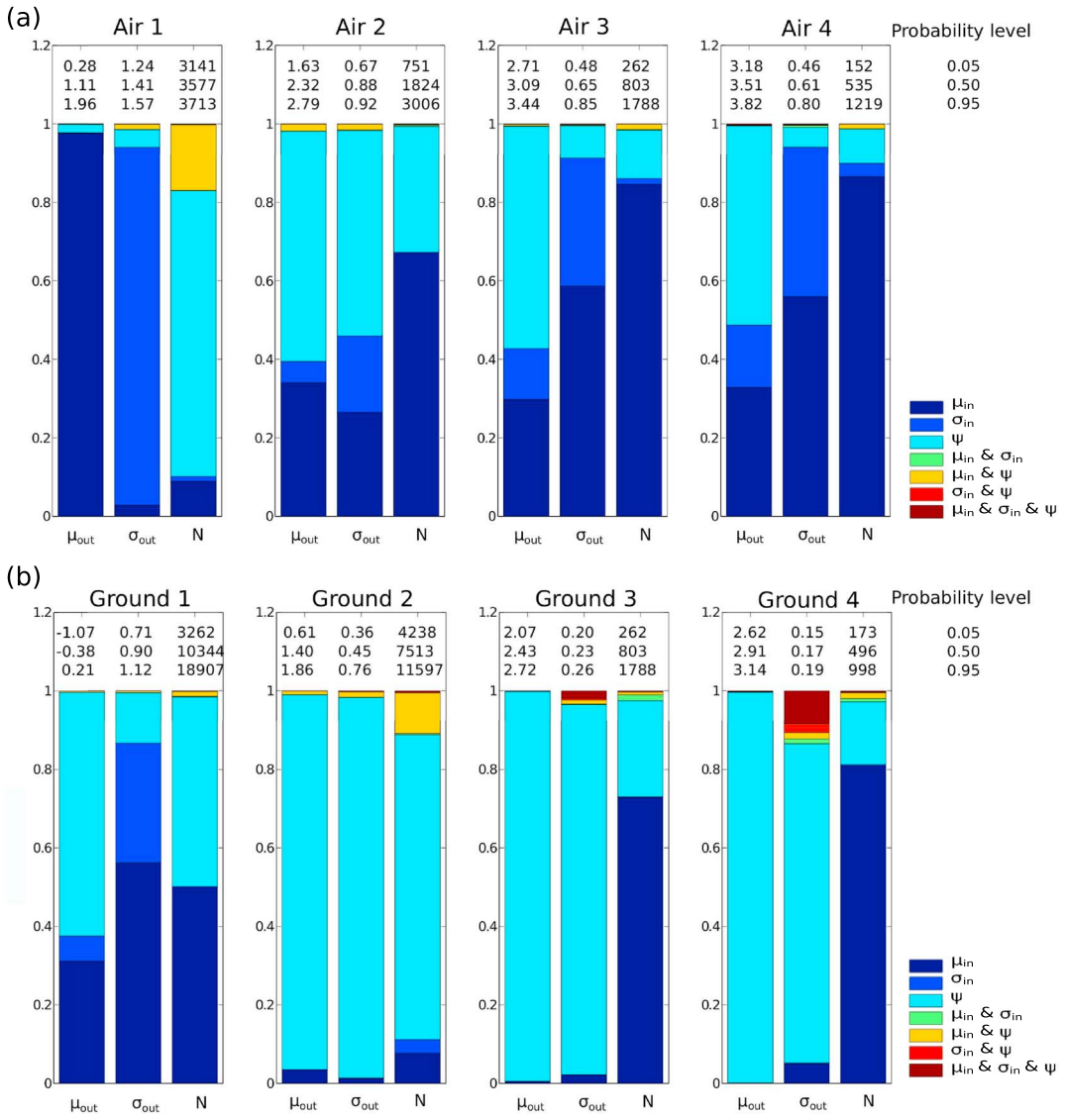

Figure 10. Main Sobol Indices of the output values (a) of the parcels dispersal in the air and (b) of the parcels deposition on the ground. The three numbers above each bar are the CFD values referred to levels 0.05, 0.5, and 0.95 for each of the output quantities. See text for further explanations

closest to the source (Air 1, with specific reference only to the standard deviation of the GSD), whereas its effect on the three output quantities is minimal in all other subdomains, especially on the ground.

In detail, as far as the aerial subdomains are concerned, Figure 10a reveals that with the only exception of the most proximal subdomain (Air 1), the initial mean diameter and the sphericity of particles appear as the main variables in determining the mean diameter of the GSD, whereas the standard deviations are mainly affected by the initial mean diameter and standard deviation itself. Vice versa, the number of parcels is mostly dependent on the initial mean diameter of the distribution. Similarly, as far as the ground plots are concerned, Figure 10b reveals that apart from the proximal deposit (Ground 1) where both the mean diameter and the sphericity show a significant effect on the three output quantities, the sphericity appears to be by far the main control of the three considered quantities with the only exception of the number of particles in the two subdomains located from 20 to 40 km from the source (Ground 3 and Ground 4).

The leading role of μ_{in} and ψ in controlling the variability of the output quantities of interest has to be related to the trend of the CDFs shown Figure 8. Above each bar of Figure 10 the CDF values corresponding to probability levels equal to 0.05, 0.5, and 0.95 are reported. These values allow to highlight the effect of the input

variability on the output quantities of interest (μ_{out}, σ_{out}, and N). Inspection of the numbers shows that even if the variability of the mean diameter and sphericity in particular seems to control the values of the output quantities of interest (see Figure 10), the variability of μ_{out}, σ_{out}, and N becomes smaller the larger is the distance from the release region (the CDFs tend to become steeper and localized around a particular value as can be seen in Figures 8 and 9). This means that the GSD observed in the subdomains becomes more independent of the initial one the farther from the release is the observation. As an example, the variability of the mean diameter of the GSD in each aerial subdomain seems to be controlled by both μ_{in} and ψ. However, whereas near the release (Air 1) μ_{out} presents a range of variability from 0.28ϕ to 1.96ϕ, corresponding to probability levels of 0.05 and 0.95, respectively, this variability is completely lost in the further subdomain (Air 4) where μ_{out} varies from 3.18ϕ to 3.82ϕ, although the influence of μ_{in} and ψ on the output variability is still present.

The leading role of particle sphericity in controlling the dispersal and deposition processes relies on the main effect it has on the drag coefficient, C_D, and thus on the influence of vertical atmospheric movements on the particle residence time. For instance, for two particles with the same diameter (assumed here equal to 5×10^{-3} m) but different sphericity, for instance, $\psi = 0.9$ and 0.5, the C_D jumps from $C_D \simeq 1$ to $C_D \simeq 4$, resulting in an increase of the residence time of about 10%. Vice versa, a variation of the initial mean diameter of the GSD does not significantly affect the value of the drag coefficient but only the amount of particles of a given size present, or deposited, at a given distance from the source.

6. Summary and Concluding Remarks

Pyroclastic particle dispersal in the atmosphere is a complex process affected by numerous sources of uncertainties. Some of them are strictly related to the nonlinear physics of the process, while some others are instead generated by the incomplete knowledge of the variables that characterize the eruptive conditions of the feeding plume. In this work we have presented a method able to quantitatively investigate the influence and role of some uncertainties in key eruption source parameters. The method is based on the adoption of a Lagrangian particle model able to describe the dispersal and deposition of particles under the action of a realistic atmospheric field generated by a mesoscale nonhydrostatic model. UQ and SA were then carried out by adopting a PCEg technique able to largely reduce the number of simulation runs and therefore the computational load needed for these analyses.

The study focused on the unavoidable source of uncertainty affecting the definition of the GSD of the pyroclastic mixture released from the volcanic plume. In particular, the adopted models allowed to quantify the propagation of this uncertainty on the parameters describing the particle size distribution estimated at different distances from the release, both in the atmosphere and on the ground. Eruptive conditions adopted referred to a weak plume event that occurred at Mount Etna on 24 November 2006, as representative of weak plume conditions, although the analysis could be easily extended to plumes of larger scale.

Based on the outcomes of the UQ and SA, these are the main conclusions of the study:

1. Ash dispersal process is able to effectively segregate particles of different sizes due to their different drag with the atmosphere. As a consequence, for a given plume height, the GSD of the mixture is mostly a function of distance from the emitting source, both airborne and on ground, independently from the original GSD of the mixture (represented herein as a Gaussian distribution).
2. For a given distance from the source, GSDs (expressed as mean diameter and standard deviation) on ground and in air are not equal. Airborne GSD is significantly finer and less sorted with respect to that estimated on ground.
3. For a given distance from source, the GSD is mostly controlled by particle sphericity. Such control is stronger on ground than in air where also the mean diameter and sorting of the initial GSD play a significant role.
4. The uncertainty range in the mean diameter of the initial GSD of the mixture is significantly reduced with increasing distance from source. Such a reduction is more effective on ground than in air.
5. The uncertainty range on the standard deviation of the GSD of the mixture is almost constant with increasing distance from source in air, whereas it drastically reduces with distance on ground.

Such findings allow to identify the variables with a larger control on the phenomenon investigated and thus deserving a deeper theoretical and laboratory investigation to better constrain the range of values to be used in numerical simulations.

The role of the input GSD as one of the main parameters governing ash dispersion and deposition has been shown also in previous works. In particular, *Scollo et al.* [2008] listed the GSD at the volcanic vent as a key factor influencing the dispersion and deposition of ash through the interaction with other factors, such as plume height, diffusion coefficient, and plume ratio (a dimensionless parameter that specifies the bottom of the particle release region as a ratio of the total height), and emphasizes its leading role especially far from the source.

From a field and observational perspective, the overall results indicate the difficulty in finding a region of the domain whose GSD is fully representative of the GSD at source. As expected, aerial regions close to the source appear to be the most representative, whereas on ground just the GSD at proximal median distance from source appears able to resemble the mean diameter of the initial GSD but not the corresponding standard deviation.

Moreover, simulation outcomes clearly show that GSDs in the atmosphere and deposited on ground can significantly differ even at the same distance from source. Significant amounts of fine particles can in fact remain suspended in the atmosphere up to remarkable distances even for weak plume events. As a consequence, the initial GSD of the mixture should be reconstructed integrating not only the ground values but also accounting for the particles still suspended in the atmosphere.

Acknowledgments
This work has been partially supported by the project MEDiterranean SUpersite Volcanoes (MED-SUV) FP7 ENV.2012.6.4-2 grant agreement 308665 (European Community). The authors acknowledge useful comments and revision by Ulrich Kueppers, an anonymous reviewer, and the Associate Editor. The data used are listed in the references, while the Lagrangian model adopted is hosted at the Volcano Modelling and Simulation gateway (http://vmsg.pi.ingv.it).

References

Adams, B. M., et al. (2006), *DAKOTA, A Multilevel Parallel Object-Oriented Framework for Design Optimization, Parameter Estimation, Uncertainty Quantification, and Sensitivity Analysis: Version 4.0 User's Manual*, U.S. Dep. of Energy.

Andronico, D., A. Cristaldi, and S. Scollo (2008a), The 4–5 September 2007 lava fountain at South-East Crater of Mt Etna, Italy, *J. Volcanol. Geotherm. Res.*, *173*(3), 325–328.

Andronico, D., S. Scollo, S. Caruso, and A. Cristaldi (2008b), The 2002–03 Etna explosive activity: Tephra dispersal and features of the deposits, *J. Geophys. Res.*, *113*, B04209, doi:10.1029/2007JB005126.

Andronico, D., S. Scollo, M. D. Lo Castro, A. Cristaldi, L. Lodato, and J. Taddeucci (2014), Eruption dynamics and tephra dispersal from the 24 November 2006 paroxysm at South-East Crater, Mt Etna, Italy, *J. Volcanol. Geotherm. Res.*, *274*, 78–91.

Bagheri, G., C. Bonadonna, I. Manzella, and P. Vonlanthen (2015), On the characterization of size and shape of irregular particles, *Powder Technol.*, *270*, 141–153, doi:10.1016/j.powtec.2014.10.015.

Barsotti, S., and A. Neri (2008), The VOL-CALPUFF model for atmospheric ash dispersal: 2. Application to the weak Mount Etna plume of July 2001, *J. Geophys. Res.*, *113*, B03209, doi:10.1029/2006JB004624.

Barsotti, S., D. Andronico, A. Neri, P. Del Carlo, P. Baxter, W. Aspinall, and T. Hincks (2010), Quantitative assessment of volcanic ash hazards for health and infrastructure at Mt. Etna (Italy) by numerical simulation, *J. Volcanol. Geotherm. Res.*, *192*(1), 85–96.

Biass, S., C. Scaini, C. Bonadonna, A. Folch, K. Smith, and A. Höskuldsson (2014), A multi-scale risk assessment for tephra fallout and airborne concentration from multiple Icelandic volcanoes—Part 1: Hazard assessment, *Nat. Hazards Earth Syst. Sci.*, *14*(8), 2265–2287.

Bonadonna, C., and B. Houghton (2005), Total grain-size distribution and volume of tephra-fall deposits, *Bull. Volcanol.*, *67*(5), 441–456.

Bonadonna, C., and J. C. Phillips (2003), Sedimentation from strong volcanic plumes, *J. Geophys. Res.*, *108*(B7), 2340, doi:10.1029/2002JB002034.

Bonadonna, C., P. Webley, M. Hort, A. Folch, S. Loughlin, and H. Puemel (2014), 2nd IUGG-WMO Workshop on Ash Dispersal Forecast and Civil Aviation, Consensual Document, International Union of Geodesy and Geophysics-World Meteorological Organization, Geneva, Switzerland.

Bonadonna, C., A. Costa, A. Folch, and T. Koyaguchi (2015), Tephra dispersal and sedimentation, in *Encyclopedia of Volcanoes*, edited by H. Sigurdsson, 2nd ed., chap. 33, pp. 587–597, Academic Press, San Diego, Calif.

Corradini, S., L. Merucci, M. Silvestri, M. Musacchio, C. Spinetti, A. Piscini, M. Buongiorno, and A. Prata (2008), SO_2 and ash plume retrievals using MSG-SEVIRI measurements. Test case: 24 November 2006 Mt. Etna eruption, in *USEReST. Second Workshop on Use of Remote Sensing Techniques for Monitoring Volcanoes and Seismogenic Areas*, pp. 1–5, IEEE.

Crowe, C., M. Sommerfeld, and Y. Tsuji (1998), *Multiphase Flows With Droplets and Particles*, CRC Press, New York.

Dalbey, K., A. Patra, E. Pitman, M. Bursik, and M. Sheridan (2008), Input uncertainty propagation methods and hazard mapping of geophysical mass flows, *J. Geophys. Res.*, *113*, B05203, doi:10.1029/2006JB004471.

de' Michieli Vitturi, M., A. Neri, T. Esposti Ongaro, S. Lo Savio, and E. Boschi (2010), Lagrangian modeling of large volcanic particles: Application to Vulcanian explosions, *J. Geophys. Res.*, *115*, B08206, doi:10.1029/2009JB007111.

de' Michieli Vitturi, M., A. Neri, and S. Barsotti (2015), PLUME-MoM 1.0: A new integral model of volcanic plumes based on the method of moments, *Geosci. Model Dev.*, *8*(8), 2447–2463, doi:10.5194/gmd-8-2447-2015.

Dorgan, A., and E. Loth (2007), Efficient calculation of the history force at finite Reynolds numbers, *Int. J. Multiphase Flow*, *33*(8), 833–848.

Douillet, G. A., K. R. Rasmussen, U. Kueppers, D. Lo Castro, J. P. Merrison, J. J. Iversen, and D. B. Dingwell (2014), Saltation threshold for pyroclasts at various bedslopes: Wind tunnel measurements, *J. Volcanol. Geotherm. Res.*, *278-279*, 14–24.

Durant, A. J., C. Bonadonna, and C. J. Horwell (2010), Atmospheric and environmental impacts of volcanic particulates, *Elements*, *6*(4), 235–240, doi:10.2113/gselements.6.4.235.

Eychenne, J., and J. L. Le Pennec (2010), Sigmoidal particle density distribution in a subplinian scoria fall deposit, *Bull. Volcanol.*, *74*(10), 2243–2249, doi:10.1007/s00445-012-0671-4.

Ganser, G. H. (1993), A rational approach to drag prediction of spherical and nonspherical particles, *Powder Technol.*, *77*(2), 143–152.

Houghton, B., and R. J. Carey (2015), Pyroclastic fall deposits, in *Encyclopedia of Volcanoes*, edited by H. Sigurdsson, 2nd ed., chap. 23, pp. 599–616, Academic Press.

Isukapalli, S. S. (1999), Uncertainty analysis of transport-transformation models, PhD thesis, The State Univ. of New Jersey.

Lee, C., and D. Leith (1989), Drag force on agglomerated spheres in creeping flow, *J. Aerosol Sci.*, *20*(5), 503–513.

Madankan, R., P. Singla, A. Patra, M. Bursik, J. Dehn, M. Jones, M. Pavolonis, B. Pitman, T. Singh, and P. Webley (2012), Polynomial chaos quadrature-based minimum variance approach for source parameters estimation, *Procedia Comput. Sci.*, *9*, 1129–1138.

Rose, W., and A. Durant (2009), Fine ash content of explosive eruptions, *J. Volcanol. Geotherm. Res.*, *186*(1), 32–39, doi:10.1016/j.jvolgeores.2009.01.010.

Scollo, S., P. Del Carlo, and M. Coltelli (2007), Tephra fallout of 2001 Etna flank eruption: Analysis of the deposit and plume dispersion, *J. Volcanol. Geotherm. Res.*, *160*(1), 147–164.

Scollo, S., S. Tarantola, C. Bonadonna, M. Coltelli, and A. Saltelli (2008), Sensitivity analysis and uncertainty estimation for tephra dispersal models, *J. Geophys. Res.*, *113*, B06202, doi:10.1029/2006JB004864.

Skamarock, W. C., J. B. Klemp, J. Dudhia, D. O. Gill, D. M. Barker, W. Wang, and J. G. Powers (2005), A description of the advanced research WRF version 2, Tech. Rep., DTIC Document, Boulder, Colo.

Sommerfeld, M., B. G. M. van Wachem, and R. Oliemans (2008), Best practice guidelines for dispersed multi-phase flow computations, Tech. Rep., ERCOFTAC.

Spanu, A., S. Barsotti, M. de'Michieli Vitturi, M. Moustaoui, A. Mahalov, and A. Clarke (2013), Kelvin-Helmholtz instabilities in volcanic clouds and their effects on ash dispersal, Abstract V23C-2862 presented at 2013 Fall Meeting, AGU, San Francisco, Calif.

Sparks, R. S. J., M. I. Bursik, S. N. Carey, J. E. Gilbert, L. Glaze, H. Sigurdsson, and A. W. Woods (1997), *Volcanic Plumes*, John Wiley, New York.

Spinetti, C., S. Corradini, and M. F. Buongiorno (2007), Volcanic ash retrieval at Mt. Etna using AVHRR and MODIS data, in *Proc. SPIE6749*, Remote Sensing for Environmental Monitoring, GIS Applications, and Geology VII, 67491M (October 30, 2007, Florence, Italy), doi:10.1117/12.752664.

Stefanescu, E., et al. (2014), Temporal, probabilistic mapping of ash clouds using wind field stochastic variability and uncertain eruption source parameters: Example of the 14 April 2010 Eyjafjallajokull eruptionö, *J. Adv. Model. Earth Syst.*, *6*(4), 1173–1184, doi:10.1002/2014MS000332.

Thompson, T. L., and N. Clark (1991), A holistic approach to particle drag prediction, *Powder Technol.*, *67*(1), 57–66.

Wiener, N. (1938), The homogeneous chaos, *Am. J. Math.*, *60*, 897–936.

Wilson, G., T. Wilson, N. Deligne, and J. Cole (2014), Volcanic hazard impacts to critical infrastructure: A review, *J. Volcanol. Geotherm. Res.*, *286*, 148–182, doi:10.1016/j.jvolgeores.2014.08.030.

Wilson, L., and T. Huang (1979), The influence of shape on the atmospheric settling velocity of volcanic ash particles, *Earth Planet. Sci. Lett.*, *44*(2), 311–324.

Xiu, D., and G. E. Karniadakis (2002), Modeling uncertainty in steady state diffusion problems via generalized polynomial chaos, *Comput. Methods Appl. Mech. Eng.*, *191*(43), 4927–4948, doi:10.1016/S0045-7825(02)00421-8.